Advanced Functional Materials

ADVANCED FUNCTIONAL MATERIALS
www.afm-journal.de

RESEARCH ARTICLE

MoS_2 Catalysts Selectively Achieve High Yield of Liquid Oxygenate from Direct Conversion of Methane via Hydroxyl Radicals

Steven L. Farrell[1] | Juan D. Jiménez[2] | Dominik Wierzbicki[1] | Jie Zhang[3] | Anna X. Chen[4] | Jordi Llorca[5] | AM Milinda Abeykoon[1] | Uddhav Kanbur[6] | Yuting Li[3] | Long Qi[3] | Shannon M. Mahurin[7] | Michelle K. Kidder[8] | Emanuele Telari[9] | Albert Bruix[9] | Arephin Islam[2] | Akhil Tayal[1] | Jorge Moncada[1] | Ayaskanta Sahu[10] | Eli Stavitski[1] | Sanjaya D. Senanayake[2]

[1]National Synchrotron Light Source II, Brookhaven National Laboratory, Upton, New York, USA | [2]Chemistry Division, Brookhaven National Laboratory, Upton, New York, USA | [3]Ames National Laboratory, Iowa State University, Ames, Iowa, USA | [4]Department of Chemistry, University of California, Berkeley, California, USA | [5]Institute of Energy Technologies, Department of Chemical Engineering and Barcelona Research Center in Multiscale Science and Engineering, Universitat Politècnica de Catalunya, Barcelona, Spain | [6]Department of Chemistry, Iowa State University, Ames, Iowa, USA | [7]Chemical Sciences Division, Oak Ridge National Laboratory, Oak Ridge, Tennessee, USA | [8]Manufacturing Science Division, Oak Ridge National Laboratory, Oak Ridge, Tennessee, USA | [9]Departament de Ciència de Materials i Química Física and Institut de Quimica Teòrica I Computacional, Universitat De Barcelona, Barcelona, Spain | [10]Department of Chemical and Biomolecular Engineering, New York University Tandon School of Engineering, Brooklyn, New York, USA

Correspondence: Steven L. Farrell (sfarrell1@bnl.gov) | Juan D. Jiménez (jjimenez1@bnl.gov) | Eli Stavitski (istavitski@bnl.gov) | Sanjaya D. Senanayake (ssenanay@bnl.gov)

Received: 16 March 2026 | **Revised:** 13 May 2026 | **Accepted:** 2 June 2026

Keywords: catalysis | molybdenum disulfide | partial methane oxidation | solid-liquid-gas interface

ABSTRACT

Directly converting methane (CH_4) into liquid oxygenates (e.g., methanol) can circumvent the cost and engineering limits of natural gas transportation and storage. However, oxygenate yields from CH_4 remain low, and sulfur present in natural gas hinders activity in most catalysts. To overcome these barriers, we employ bulk molybdenum disulfide (MoS_2), a low-cost, robust catalyst which selectively produces large quantities of liquid oxygenates (>900 μmol/g_{cat}•hr) from methane in the presence of hydroxyl ($OH^{\bullet}$) radicals produced from dilute hydrogen peroxide (H_2O_2) at 75°C. Under realistic reaction conditions, MoS_2 partially and reversibly adopts a metastable, more electrically conductive phase (1T') that can only be observed through in situ structural probes. Herein, we elucidate that redox synergy between H_2O_2 and MoS_2 produces active $OH^{\bullet}$ radical species that selectively transform CH_4 to surface methoxy species at the gas-solid liquid interface, leading to the unitary production of liquid oxygenate at a rate competitive with more costly precious metal catalysts, without additional catalyst preparation steps.

1 | Introduction

Direct conversion of methane (DCM) to liquid oxygenates such as methanol greatly reduces the cost and complexity of natural gas storage and transmission, especially compared with indirect routes through energy-intensive syngas (CO and H_2) formation [1]. This process can also produce valuable products from waste by utilizing stranded CH_4, which is economically infeasible to store and often flared off [2, 3]. Recent progress in the DCM field has been made using liquid-mediated processes, with oxidants such as hydrogen peroxide (H_2O_2) [4–6], in situ H_2O_2 generation [7], and chemical looping [8]. Achieving viable yields via this conversion is challenging even in the presence of a catalyst due to the strong C—H bonds in CH_4 [9]. To

this end, liquid oxygenate yields from CH_4 remain low, with higher turnover catalysts overoxidizing CH_4 or its intermediate products and thus producing large amounts of undesired CO_2 byproduct [5, 10]. Recent reports show the excellent potential for methane conversion using non-precious metal catalysts in H_2O_2 systems [6]. Another major hurdle in the adoption of DCM is the quality of natural gas. Maximum benefit arises from this process when employed at the point of natural gas production, meaning the grade of gas is limited by the purification process units present on site. Natural gas composition varies between production sites, with many sources containing hydrogen sulfide (so-called "sour gas") that can affect the lifespan of catalysts containing sulfur-susceptible precious metals or even common metals like iron, requiring purification via gas sweetening [11–14]. An ideal DCM catalyst would therefore need to be resilient to sulfur, especially in processes where sweetening is limited or unavailable.

A material that can bridge this issue is molybdenum disulfide (MoS_2), a low-cost and Earth-abundant transition metal dichalcogenide (TMD) with a long history as an industrial catalyst that still attracts thorough research attention [15, 16]. Frequently employed in processes where deactivation by sulfur is a risk due to its high sulfur tolerance, MoS_2 demonstrates high activity in a number of reactions, including hydrogenolysis of fuel feedstocks [17], water splitting [18], and deoxygenation of lignin into biofuels [19]. Mo-based catalysts have rich chemistry for interacting with natural gas species even in nonmetallic compounds, and are thus very attractive for converting methane [20]. MoS_2 has recently shown promise as a DCM catalyst under mild aqueous conditions using molecular oxygen, using undercoordinated edge sites in nanoscale MoS_2 to drive methane conversion [21]. While the edge sites of MoS_2 are typically considered catalytic, the remaining area (the basal plane) is semiconducting and inert for many reactions [15–19, 21]. As a result, MoS_2 often requires tailored modification or treatment to activate it for a number of reactions [22, 23]. Several reports demonstrate the oxidative species formation and electron transport improvements in bulk MoS_2 treated with H_2O_2 [24–26]. Particularly, MoS_2 self-generates selectively active radical oxygen species, such as $OH^{\bullet}$, from H_2O_2, a key intermediate in DCM [5, 25, 27]. This opportunity for synergy between process and catalyst in DCM has, to the best of our knowledge, heretofore not been reported.

In this work, we investigated unmodified bulk MoS_2 as a low-cost, practical DCM catalyst that excels in aqueous H_2O_2-containing media, with activity competitive with precious metal catalysts. We employed a suite of synchrotron-based spectroscopy and scattering techniques to probe real-time MoS_2 structural and electronic behavior under working conditions and to elucidate the catalyst role in DCM. This approach, which incorporates various complementary ex situ and in situ characterization methods, demonstrates the catalyst-oxidant synergy involved in the structure-activity relationship. By integrating these aspects with reactor kinetics studies, we demonstrate the effectiveness of this catalyst and build the knowledge base for further DCM catalyst optimization and improvement. Our multimodal approach of spectroscopy, kinetics, and theory highlights the critical dual role of H_2O_2 for oxidizing methane and inducing metallic behavior in MoS_2 as the driving force behind this reaction.

2 | Results and Discussion

2.1 | Methane Conversion and Radical Formation Activity

MoS_2 exhibited remarkable conversion of CH_4 into methylperoxide (CH_3OOH), a metastable liquid oxygenate, with 100% selectivity toward CH_3OOH in a batch reactor system at 75°C in 60 min. (Figure 1a). The liquid oxygenate yield of 946 ± 91 μmol/g_{cat} demonstrates that the activity of MoS_2 is competitive with reported precious metal-based catalysts used for DCM (Tables S1–S3). For comparison, we performed the same test on nanoscale MoS_2 (synthesized from our previous work) [28] and found that under these conditions, bulk MoS_2 outperformed nanoscale MoS_2 (Figure S1). Tabulation of all carbon products detected in this reaction are listed in Table S3. MoS_2 does not overoxidize CH_4 into CO_2 under these conditions, a common trade-off for many high-yield catalysts, nor does it convert to other oxygenate products. At higher temperature (85°C), CO_2 and methanol (CH_3OH) begin to appear. The formation of CO_2 is attributed to the further oxidation of the product CH_3OOH in the presence of H_2O_2. The rate of DCM and product selectivity is also a function of the amount of available reactive oxygen species (Figure 1b), where the CH_3OOH selectivity scales with the H_2O_2 initial concentration. Excess H_2O_2 contributes to more solvated $OH^{\bullet}$ species and higher CH_3OOH selectivity, whereas lower concentrations of H_2O_2 lead to less solvated $OH^{\bullet}$ and thus result in more CH_3OH production. Peroxide decomposition titration studies reveal that MoS_2 decomposes H_2O_2 at 75°C, albeit slower and generating a milder oxidative environment compared to palladium-based catalysts at ambient temperature (Figure 1c) [5]. As such, the appearance of CH_3OH begins at 85°C, which we attribute to lower $OH^{\bullet}$ concentration in the system after some time has elapsed, as a result of accelerated decomposition of H_2O_2 at temperature over MoS_2.

Time-resolved reactor studies (Figure 1d) show the appearance of both CH_3OH and CO_2 with extended reaction time. The appearance of CH_3OH likely stems from the decreasing H_2O_2 concentration over time. After 180 min. of reaction time in batch, the product mixture remains relatively the same measured at 360 min., implying that the reaction has quenched. Product formation ceases, and the formed products (CH_3OOH, CH_3OH, CO_2) are stable. As the total conversion of CH_4 is low (0.35%), we attribute this quenching to the consumption of H_2O_2 sometime after 120 min.; as H_2O_2 decomposes, O_2 is detected in the head gas but is unlikely to act as an oxidant in this system as no further conversion occurs. This contrasts with edge-rich nanoscale MoS_2 previously reported and is likely due to the lower density of edge sites in bulk MoS_2 [21]. Irreversible deactivation of the catalyst is ruled out, as MoS_2 is reusable over multiple cycles, demonstrating its capability for use in multiple successive runs in fresh H_2O_2 with no discernible loss of activity (Figure S2). To verify the overoxidation of CH_3OH as an avenue for CH_3OOH or CO_2 formation, an equivalent amount of CH_3OH was added in place of CH_4 (under pressurized inert gas) where neither CH_3OOH nor CO_2 were formed, showing that both CH_3OOH and CO_2 both arise from a methane-derived intermediate and not from the sequential readsorption of CH_3OH. This overall demonstrates that CO_2 formation arises from further interaction

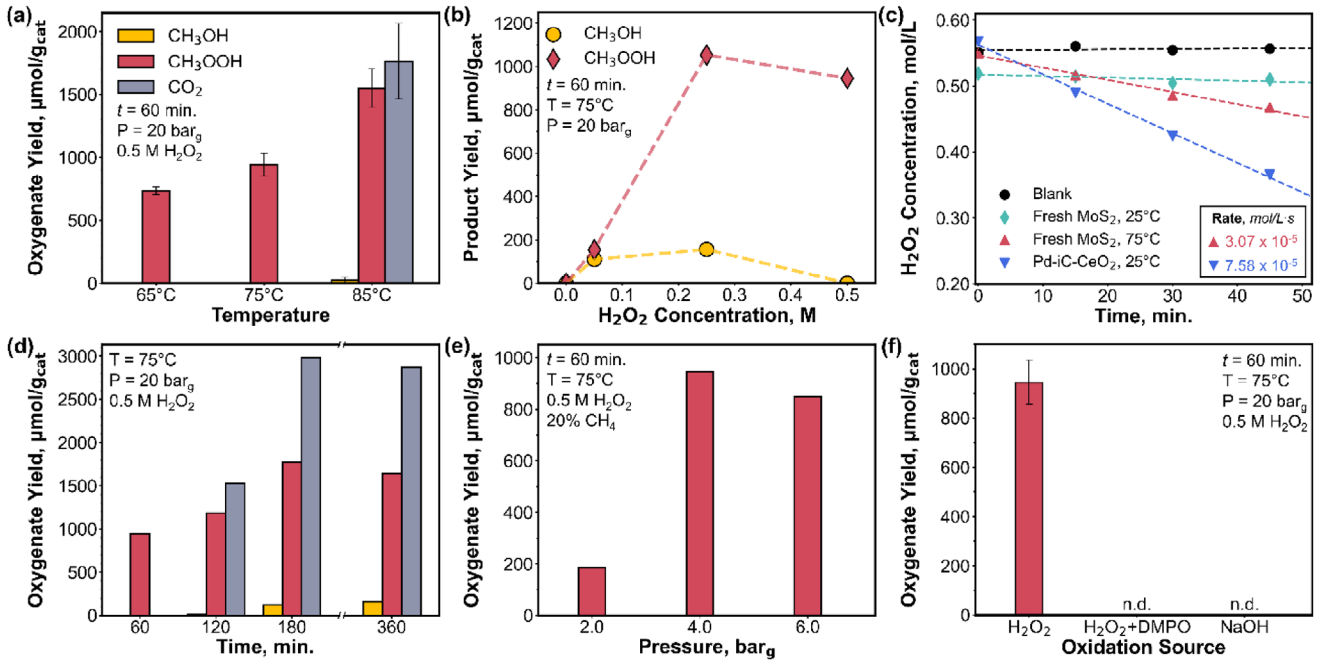

FIGURE 1 | (a) Temperature studies, (b) peroxide concentration studies, (c) temporal decomposition of H_2O_2 over catalyst compared with a similar test conducted over a milled Pd-ceria catalyst (Pd-iC-CeO_2) [5], (d) temporal reaction studies from 60 to 360 min., (e) total pressure effect studies, (f) effect of different oxidative environments using H_2O_2 with 0.1 M DMPO and 0.5 M NaOH showing no products detected at 75°C after 60 min. All runs were conducted with 2 mg MoS_2 in 15 mL of H_2O_2 solution, pressurized with 20% CH_4/10% Ar/Balance He, for 60 min. Specific conditions are noted in each figure. *Note*: "n.d." = not detected.

between H_2O_2 and CH_3OOH, and not through CH_3OH oxidation or a mechanism with O_2.

Varying the pressure of the total batch (Figure 1e) reveals a dependence on elevated pressure up to 20 bar_g (4 bar_g CH_4). Activity increases significantly when raising from 10 to 20 bar_g (2 to 4 bar_g CH_4), suggesting activity may be limited by low methane solubility in water [29]. Increasing the pressure to 30 bar_g (6 bar_g CH_4) does not give a further activity increase. Regarding the active oxidation component of H_2O_2, we note (vide infra) the absence of $OO^{\bullet}$ and $OOH^{\bullet}$ species in our electron paramagnetic resonance (EPR) analysis. As H_2O_2 decomposition results in a wide array of both $OH^{\bullet}$ and OH^-, the dependence upon $OH^{\bullet}$ radical species specifically as the driving oxidant is demonstrated in Figure 1f; wherein adding 5,5-dimethyl-1-pyrroline-*N*-oxide (DMPO), an $OH^{\bullet}$ radical trap, to the H_2O_2 solution completely quenched the MoS_2 activity by removal of $OH^{\bullet}$. Alternatively, substituting NaOH as a source of OH^- ions in place of H_2O_2 at an equivalent concentration yielded no activity, showing that OH^- anions are not involved in the reaction mechanism and directly implicating the need for specifically $OH^{\bullet}$ to drive the DCM chemistry. We also note the absence of either CO or C_2H_6 formation from CH_4, implying the reaction does not proceed through an alternate pathway of CO hydrogenation or CH_4 dimerization, respectively. Formic acid (8.1 ppm) and formaldehyde (9.1 ppm) [30] were not observed either as a gas, a monomer in solution, or in hydrated form (methanediol; 4.8 ppm). To the best of our ability, methanediol may be ruled out as a product in appreciable amounts. However, overlap with the water signal in 1H NMR makes it such that its absence cannot be fully confirmed [31].

To study the formation of radical species generation and behavior on MoS_2, we probed this system with EPR under reaction conditions [32]. Short-lived free radicals were identified using DMPO as a spin trapping agent under 5 bar CH_4 with MoS_2, deuterium oxide (D_2O), and H_2O_2 heated to 75°C. MoS_2 drives the appearance of hydroxyl ($OH^{\bullet}$) radicals, evidenced by a 1:1:1 triplet signal at $g \sim 2.014$ (Figure 2a). This triplet signal matches the simulation (Figure 2b) of HDMPO-OH (2,2-dihydroxy-5,5-dimethyl-1-pyrrolidinyloxy, Figure S3), an adduct of DMPO which arises from interaction with multiple $OH^{\bullet}$ radicals [33, 34]. The baseline signal of DMPO in H_2O_2 without catalyst shows a small signal containing a quartet and a sextet, attributed to DMPO-OH from H_2O_2 auto-decomposition and spontaneous radical formation in water exposed to ambient light [35]. At ambient temperature, a sextet appears, with a quartet appearing at elevated temperature from natural H_2O_2 decomposition (Figure S4). MoS_2 increases the formation of hydroxyl radicals over the baseline from auto-decomposition, as indicated by the formation of the HDMPO-OH triplet; this occurs without the presence of CH_4. Once CH_4 is added, the g-factor shifts lower in magnetic field. This indicates significant methane interaction with the $OH^{\bullet}$ in the reaction environment and directly demonstrates the critical role of the $OH^{\bullet}$ formation in DCM over MoS_2. This triplet signal was tracked over the course of 60 min (Figure 2c); the HDMPO-OH triplet appears soon after the mixture is combined, and the intensity of this triplet quickly grows to a maximum before slowly decaying. The formation of this adduct is associated with the $OH^{\bullet}$ radicals generated from H_2O_2, followed by their consumption over time. This suggests that $OH^{\bullet}$ is the primary radical through which this reaction proceeds, rather than through peroxyl ($OOH^{\bullet}$) radicals,

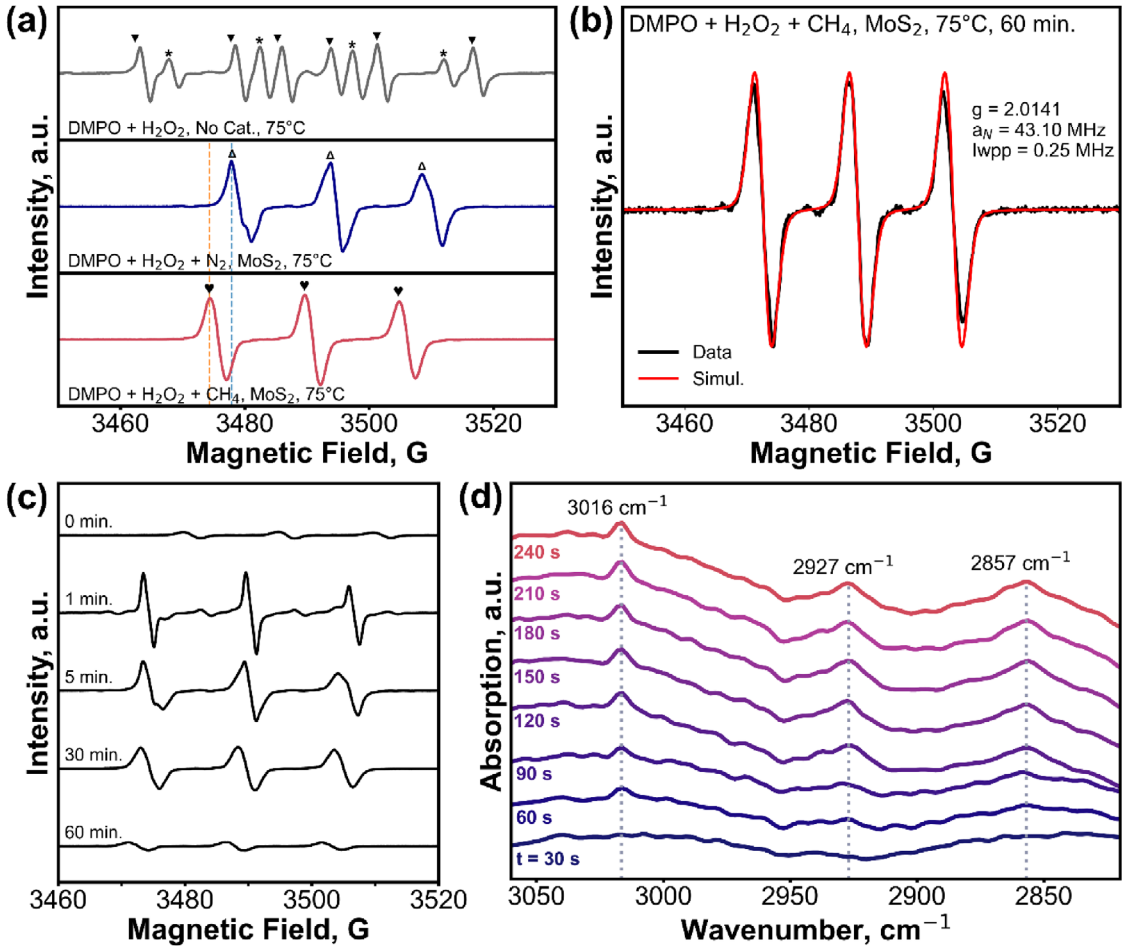

FIGURE 2 | In situ analysis of surface species and radicals: (a) control experiments of DMPO conducted in H_2O_2 (dotted lines added to highlight peak shift), (b) simulation of HDMPO-OH showing fit to triplet signal after 60 min., (c) time-resolved EPR conducted under CH_4 (1.5 bar_g), H_2O_2 (0.5 M), and MoS_2 (2 mg) in D_2O, (d) time-resolved ATR measured in 30 s intervals under CH_4 (1.5 bar_g) and H_2O_2 (0.5 M) with peak assignments for CH_4 (3016 cm^{-1}) and CH_3O^* (2927, 2857 cm^{-1}). EPR assignments: water ionization sextet (▼) [35], DMPO-OH quartet (*), HDMPO-OH triplet (Δ,♥).

which form a distinct sextet DMPO adduct, as the formation of methylperoxide might initially imply.

We examined the reaction surface chemistry of MoS_2 and associated reaction intermediates of CH_4 conversion through attenuated total reflection infrared spectroscopy (ATR-IR, Figure 2d) in a 0.5 M H_2O_2 solution and under CH_4 gas flow at 75°C. A gaseous CH_4 band (3016 cm^{-1}) appears once the CH_4 gas flow saturates the liquid phase, while characteristic bands for asymmetric (2928 cm^{-1}) and symmetric (2856 cm^{-1}) methoxy C—H stretching appear within 60 s of reaching 75°C and grow temporally, indicating continued liquid oxygenate formation [36, 37]. These bands are absent when MoS_2 is not present, while the CH_4 band remains; replacing CH_4 with He yields no peaks in this region (Figure S5). The appearance of methyl only in the presence of MoS_2 suggests that the peroxide and MoS_2 both share a role in activation of CH_4. Upon shutting off the CH_4 flow and sealing the ATR cell, making a batch in situ measurement, we observe the consumption of CH_3O^* as a function of time with simultaneous formation of CO_2, which further corroborates that the reaction intermediates, such as CH_3O^*, are susceptible to overoxidation (Figure S6). The formation of methoxy is significant at the operating pressure of the ATR (1.5 bar_g), comparable to the CH_4 partial pressure (4 bar_g) of the reactor experiments; this also suggests that elevated pressure is not a prerequisite for activation. The combination of in situ EPR and ATR-IR suggests that the mechanism likely proceeds via the formation of CH_3O^* intermediates, through an initial reaction between $OH^•$ and CH_4, forming CH_3O^*, which then reacts with a second $OH^•$ species to form CH_3OOH. The sequential activation of CH_3O^* with two $OH^•$ species to form CH_3OOH is corroborated by the H_2O_2 concentration dependence for CH_3OH vs CH_3OOH formation, where higher H_2O_2 concentration, i.e., higher $OH^•$ concentration, results in more CH_3OOH while lower H_2O_2 concentration results in the formation of CH_3OH.

2.2 | Catalyst Structure and Interaction With H_2O_2

Probing the ex situ structure of the MoS_2 catalyst before and after DCM, we observe clear evidence of partial exfoliation of the layered structure, while the ordered hexagonal intralayer structure is maintained. High-angle annular dark-field scanning tunneling electron microscopy (HAADF-STEM, Figure 3a) shows natural semiconducting (2H) MoS_2, visible in the fresh material

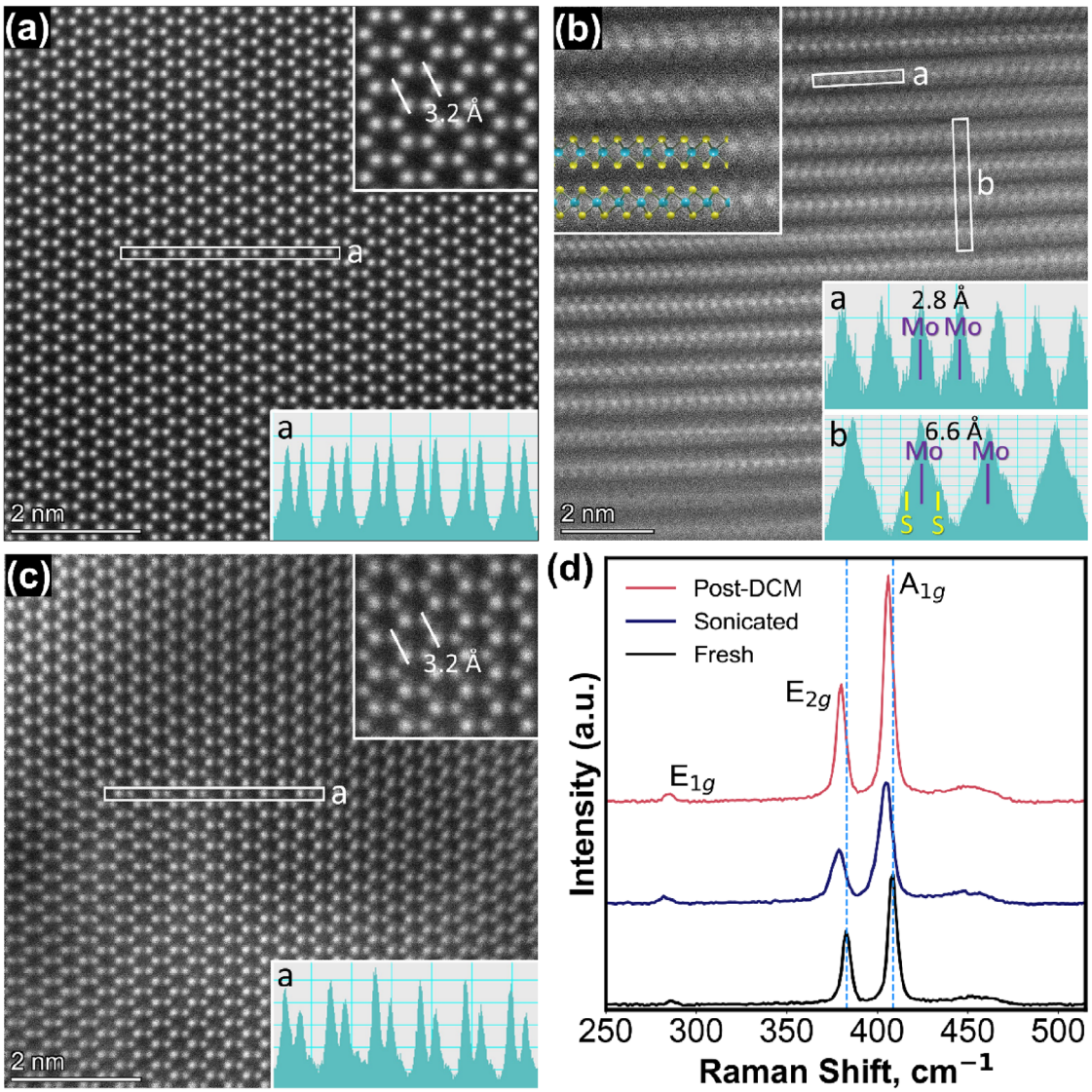

FIGURE 3 | Structure analysis of MoS_2 catalyst by HAADF-STEM: (a) fresh bulk MoS_2 along <001> and (b) along <100>, (c) MoS_2 after brief sonication of use in DCM at 75°C along <001>, (d) Raman spectroscopy. Post-DCM catalysts run after 60 min. in 20 bar_g (20% CH_4/balance inerts), 0.5 M H_2O_2 at 75°C, then centrifuged and washed with DI water and dried under vacuum for at least 24 h before measurement.

as a regular hexagonal pattern of Mo and S atoms. In the z-plane, layers of MoS_2, observed along the (100) plane with an interlayer distance of 6.6 Å (Figure 3b), are bound only by van der Waals forces [16]. Prior to reaction, the catalyst is dispersed in the 0.5 M H_2O_2 solution by brief sonication. This sonication also shows an exfoliating effect, as microscopy performed on MoS_2 after brief sonication in dilute H_2O_2 (Figure 3c) shows evidence of partial exfoliation into smaller sections by separating layers, with a loss of contrast consistent with few-layer MoS_2. A potential mechanism for this action is the intercalation of layers with H_2O_2, which can decompose to form gaseous O_2 and $OH^{\bullet}$ radicals. Rapid expansion between layers overcomes the van der Waals forces holding them together, separating them. This previously reported mechanism [25, 38, 39] showed in some cases a partial transformation from the stable 2H polytype to the metastable, metallic octahedral (1T) polytype, primarily in the form of the distorted (1T') arrangement [40, 41]. After 60 min in DCM, the catalyst retains the same general structure (Figure S7) with a similar contrast loss emphasizing an exfoliated structure.

Raman spectroscopy (Figure 3d) further supports that the structure of MoS_2 is preserved, evident in the presence of the characteristic E_{1g} (286 cm^{-1}), E_{2g} (383 cm^{-1}), and A_{1g} (408 cm^{-1}) peaks. A shift in the E_{2g} and A_{1g} peaks to lower wavenumbers after sonication and use in DCM are consistent with partial exfoliation of the MoS_2 layers [39]. Notably, we do not observe significant peaks in the region of 800–1000 cm^{-1} (Figure S8), which normally would indicate the presence of molybdenum oxide (MoO_x) or molybdenum oxysulfide ($MoOS_x$) formation via Mo = O vibrations, nor do we observe characteristic peaks for the 1T' phase of MoS_2 [20, 25].

We further probed the structure via X-ray diffraction (XRD, Figure 4a) and pair distribution function (PDF, Figure 4b). The diffraction patterns of both fresh and post-DCM catalysts match well with the 2H-MoS_2 structure and with each other, with no indication of significant structural changes. In the post-DCM catalyst, the primary XRD peak representing the (100) plane is smaller relative to other peaks when compared with fresh

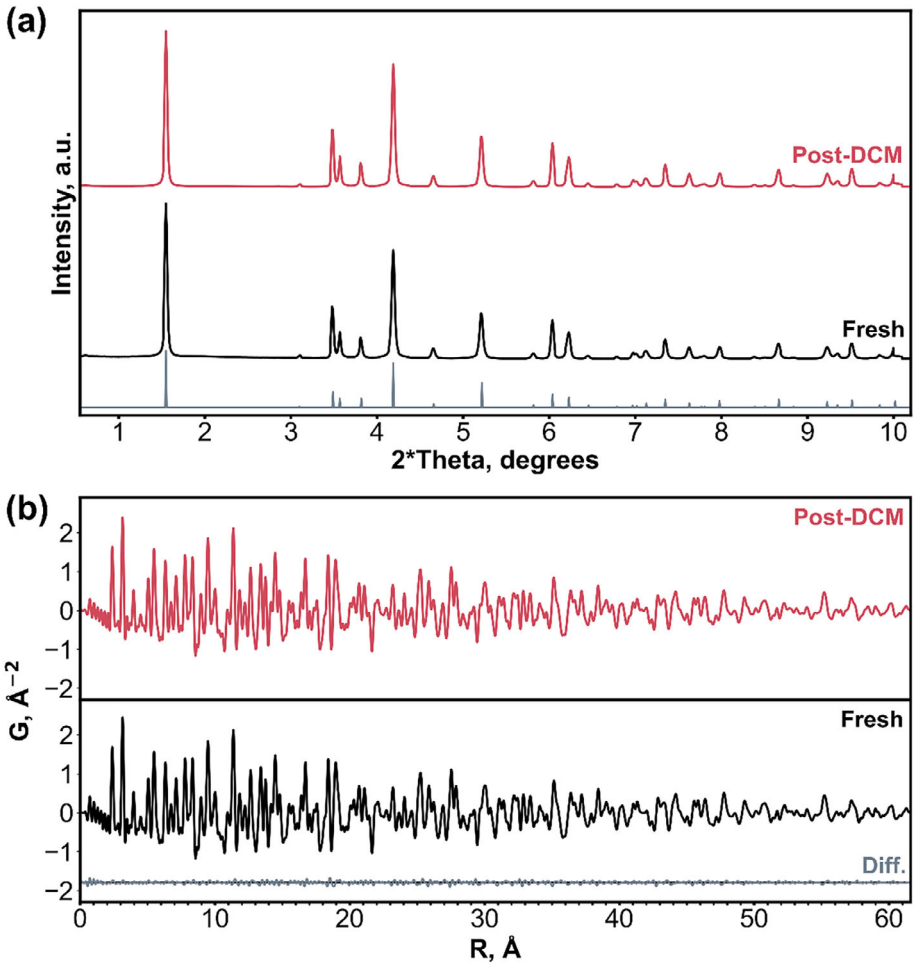

FIGURE 4 | Ex situ XRD (a) and PDF (b) measurements of MoS_2 before (black) and after 60 min. of use in DCM at 75°C (red). Sonicated material was briefly sonicated in 0.5 M H_2O_2, then collected and dried for measurement. XRD measurements are normalized to their largest peak and were conducted with a wavelength (λ) of 0.1665 Å. Reference peaks (grey) are based on COD-9007660 [43]. In PDF, the measurement difference between the fresh and post-DCM catalyst is plotted in grey below the fresh catalyst.

MoS_2 (Figure S9). This implies there are fewer interlayers as a result of exfoliation, consistent with HAADF-STEM and Raman spectroscopy. In PDF, fresh MoS_2 exhibits long-range order, with prominent peaks at 2.42 and 3.15 Å consistent with the average Mo—S and Mo—Mo distances in 2H-MoS_2, respectively (Figure S10) [42]. Post-DCM (60 min, 75°C) catalyst maintains the general structure, with peak locations unchanged from the fresh material and no signs of atomic-level distortions or changes. While the 1T' phase is partly observed in situ (vide infra), likely this metastable phase is not preserved during cleaning and vacuum-drying of the post-DCM catalyst in preparation for measurement; thus the catalyst reverts to its most stable form.

Critically, we note the lack of regular sulfur vacancies or oxidation of the structure, identifying MoS_2 as a robust catalyst for this process as measured by Raman, HAADF-STEM, and PDF. Additionally, ICP was conducted on the remaining mother liquor, filtered to remove catalyst, and no sulfur leaching was detected. Extended X-ray absorption fine structure (EXAFS) of fresh and post-DCM catalyst measured ex situ showed no discernible loss of Mo—S coordination during reaction (Figure S11; Table S4).

X-ray photoelectron spectroscopy (XPS) was carried out ex situ on fresh (Figure 5a) and post-DCM catalyst (Figure 5b), the latter of which was dried under vacuum after use to remove residual peroxide solution, finding no shifting of peaks between samples that would indicate significant oxidation or retention of the 1T' phase after removal from reaction [17, 40]. Both catalysts show Mo^{4+} states primarily with some Mo^{6+} states present. A very small peak attributed to minor sulfur oxidation is noted in the post-DCM catalyst (169.5 eV), but no sulfates or molybdenum sulfoxide are detected in bulk techniques such as Raman (Figure 3d) or S K-edge XANES (Figure 7, vide infra). We attribute this to mild oxidation present only at the surface. The oxygen content represents less than 3 at.%, and is unlikely to make a significant contribution to the catalyst behavior or structure. The atomic ratios of S to Mo (Table 1) show that the atomic ratio of approximately 2:1 is maintained between fresh and post-DCM catalysts, with no indication of vacancy formation through sulfur loss.

2.3 | Catalyst Behavior in DCM

While the structure of MoS_2 is relatively similar before and after use in DCM, X-ray absorption spectroscopy (XAS) conducted

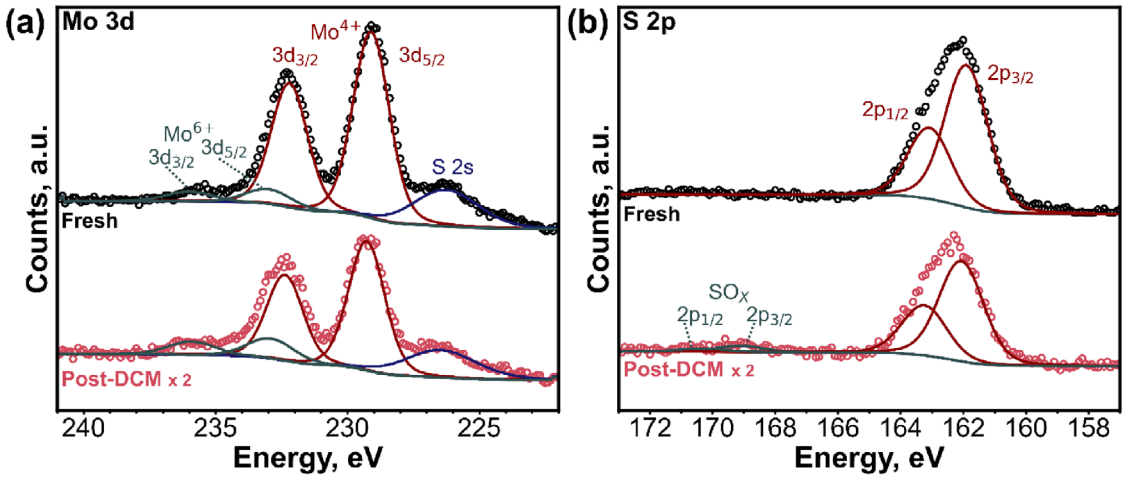

FIGURE 5 | XPS scans of Mo (a) and S (b) surface chemical states. Both fresh and post-DCM catalysts show a mixture of predominantly Mo^{4+} states with a small number of Mo^{6+} states. A small amount of surface oxygen is detected on sulfur, forming a small sulfate peak at 169.5 eV in the catalyst after reaction. No significant peak shifts are detected between the fresh and post-DCM catalysts.

TABLE 1 | Atomic percentages of Mo and S in fresh and post-reaction catalyst samples, as measured by XPS.

Sample	Mo atomic %	S atomic %	S:Mo Ratio
Fresh MoS_2	32.57%	67.42%	2.07
Post-DCM MoS_2	31.63%	68.36%	2.16

at the Mo and S K-edges to probe the electronic state and local structure of MoS_2 under realistic high-pressure reaction conditions shows structural and electronic changes in situ. Catalysts were sonicated briefly in H_2O_2 solution and dried before measurement. Dilute H_2O_2 (0.05 M) was pressurized with 20 bar_g CH_4 and introduced to the catalyst at pressure using a custom-fabricated high-pressure reaction cell (Figure S12). As CH_4-saturated H_2O_2 solution is introduced, the Mo K-edge is reduced relative to the fresh catalyst, as observed through the decrease in absorption energy in X-ray absorption near-edge structure (XANES, Figure 6a). This reduction intensifies with increasing temperature. This shift is not seen when using CH_4 and deionized water in place of H_2O_2 (Figure S13). When CH_4 is replaced with an inert (N_2), the Mo K-edge absorption energy does not shift drastically under the influence of H_2O_2 (Figure 6b), but non-reductive changes observed in the XANES are present only when H_2O_2 is introduced, emphasizing the synergy in this triphasic system. This is specifically evident in the location of the white lines (maxima), denoted in Figure 4b by dotted hash marks, of bulk MoS_2 (20 020.0 eV) and MoS_2 under H_2O_2 (20 022.2 eV) regardless of absorption energy. This species-dependent redox behavior highlights the role of CH_4 in electron donation, indicating a direct electronic interaction between CH_4 and the catalyst surface, and the influence imparted by H_2O_2.

EXAFS from the Fourier transform of the spectra yields two distinct shells for Mo—S and Mo—Mo coordination (Figure 6c), with a shift to lower radial distance in the second shell at 75°C. Fitting the EXAFS data with Artemis reveals a contribution to the second shell from the 1T' MoS_2 structure that cannot be satisfied by 2H-MoS_2 alone (Figure 6d; Table S5) [44]. The partial shift from 2H- to 1T'-MoS_2 in the presence of dilute H_2O_2 is consistent with prior literature reports [44, 45]. Comparing XANES and EXAFS with a 1T'-MoS_2 reference, synthesized according to prior literature [46], shows a similar shift in white-line and second coordination shell in the in situ catalyst (Figure S14). A partial 1T'-MoS_2 starting material would have higher electrical conductivity and potentially an active basal plane, which emphasizes the synergistic role of H_2O_2 in MoS_2 activation. This reduction and distortion are short-lived due to the metastable nature of 1T'-MoS_2 and cannot be detected in ex situ XAS (Figure S15), HAADF-STEM (Figure 3a–c), or Raman spectroscopy after the used catalyst is dried (Figure 3d). Thus, we see that the electronic interaction of CH_4 with MoS_2 is not inextricably linked to metallic character, but an active basal plane would drive turnovers via an increase in accessible active catalyst surface area.

In situ XAS of the S K-edge indicates sulfur within MoS_2 is highly sensitive to its environment. Relative to bulk MoS_2, introducing CH_4 increases the S^{2-} peak intensity (Figure 7a); while this has been previously proposed to indicate formation of sulfur vacancies [47], no evidence of vacancies was noted in the techniques discussed previously. We instead hypothesize that, in this case, it indicates further S3p – Mo4d hybridization consistent with the reduction observed in the Mo K-edge. Again, this electronic effect is driven by H_2O_2, as the inclusion of CH_4 only slightly increases the intensity of the hybridization peak relative to H_2O_2 and N_2 (Figure 7b). This shows that Mo atoms are driving the interactions with CH_4, evidenced by its notable redox change under CH_4, while S likely contributes a more subtle electronic interaction. The lack of a S^{6+} peak (~2481 eV) implies no sulfate is formed on the surface, although it does not necessarily indicate that the sulfur surface is inert to oxygen. Due to the close proximity of the Mo L_3-edge (~2520 eV), EXAFS of the S K-edge cannot be studied to determine sulfur nearest neighbors.

We have carried out Density Functional Theory (DFT) calculations to characterize the formation of $OH^{\bullet}$ radicals on MoS_2 and to differentiate the impact of MoS_2 polytype on radical

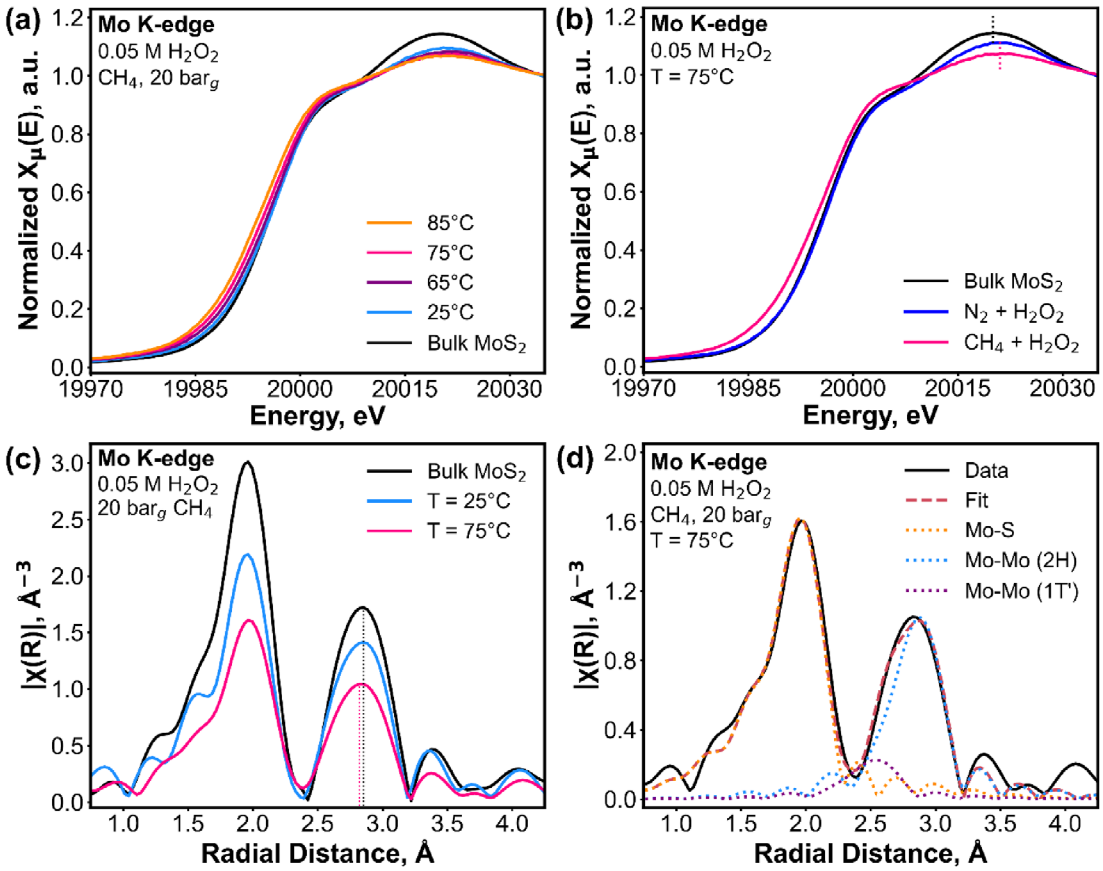

FIGURE 6 | In situ X-ray absorption spectroscopy measurements at the Mo K-edge: (a) XANES at varying temperatures, conducted under 0.1 mL/min flow of 0.05 M H_2O_2 and 20 bar_g CH_4, (b) XANES conducted under similar conditions, with and without CH_4, (c) EXAFS at varying temperatures highlighting the shrinking radial distance in the second shell, (d) EXAFS fitting of catalyst measured in 0.05 M H_2O_2, 20 bar_g CH_4 at 75°C, showing the fit of 1T' and 2H Mo—Mo paths to the structure at temperature. All measurements compared with fresh bulk MoS_2 for reference.

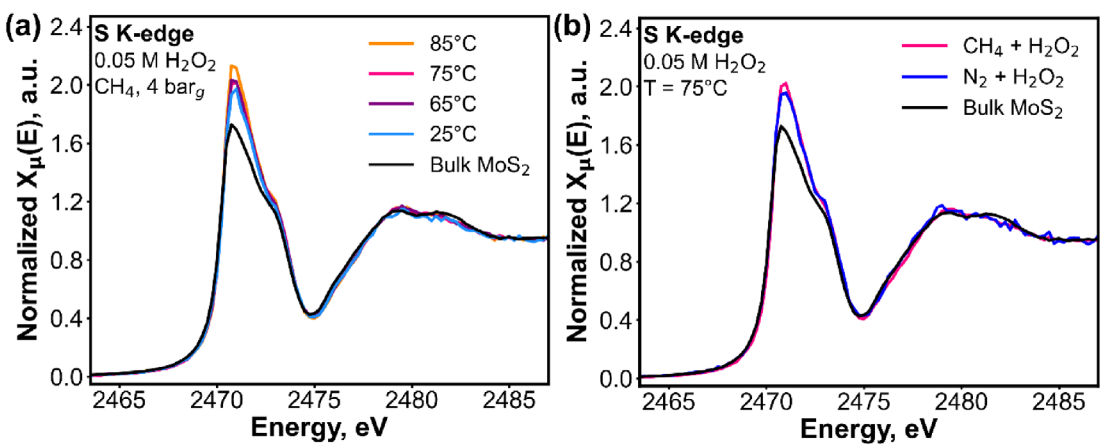

FIGURE 7 | In situ X-ray absorption spectroscopy measurements at the S K-edge: (a) XANES at varying temperatures, conducted under 0.1 mL/min flow of 0.05 M H_2O_2 and 4 bar_g CH_4, (b) XANES comparing in situ measurements with and without CH_4. All measurements compared with fresh bulk MoS_2 for reference.

formation as a driver of methane conversion chemistry (see computational details in the Supporting Information). As the edge area of bulk MoS_2 used in these studies is much less than the area of the basal plane, we have therefore investigated $OH^{\bullet}$ radical formation on the basal planes of both 2H-MoS_2 and 1T'-MoS_2. The reaction paths corresponding to the adsorption and dissociation of H_2O_2 into two $OH^{\bullet}$ are shown in Figure 8. The formation of $OH^{\bullet}$ radicals on the 2H phase is both kinetically and thermodynamically unfavorable; $OH^{\bullet}$ radicals are 1.07 eV less stable than adsorbed H_2O_2, and the dissociation reaction

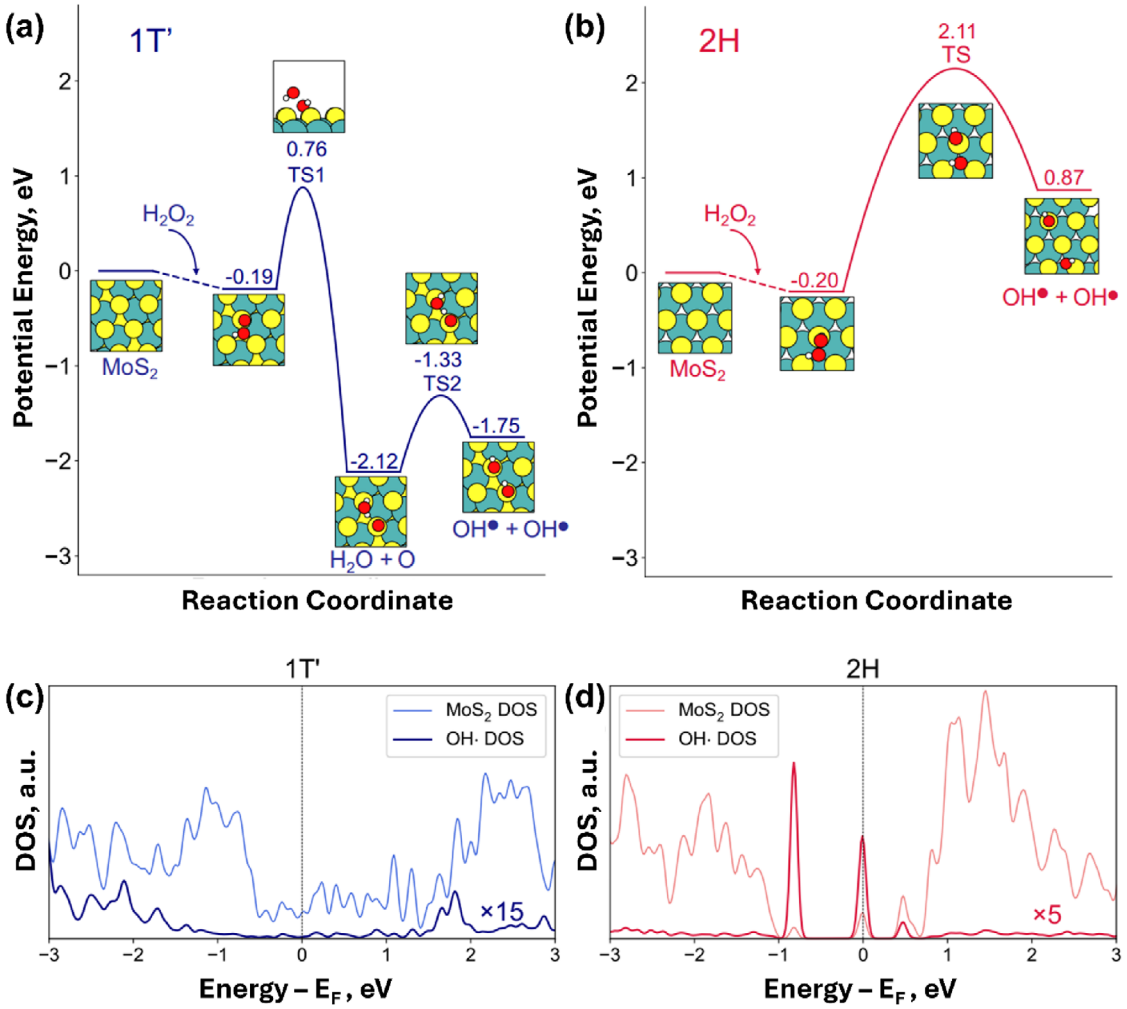

FIGURE 8 | Reaction pathways from DFT calculations for the adsorption of H_2O_2 and dissociation into OH radicals on the basal plane surface of the 1T' (a) and 2H (b) phases of MoS_2. Density of states projected on MoS_2 and OH$^\bullet$ states for 1T' (c) and 2H (d) demonstrate the metallic character of the 1T' material and the associated OH$^\bullet$. The dotted vertical line indicates the location of the Fermi energy level (E_F).

involves a barrier of 2.31 eV. Conversely, OH$^\bullet$ radicals are −1.56 eV more stable than adsorbed H_2O_2 on the 1T' phase, and their formation involves low-energy barriers for the first reaction to co-adsorbed H_2O and O (0.95 eV) and the subsequent reaction to form two OH$^\bullet$ (0.78 eV). These results indicate that the presence of 1T' phase domains in the basal plane of MoS_2 results in the formation and availability of OH$^\bullet$ radicals in a way that cannot be achieved through the 2H-MoS_2 basal plane alone and highlights the synergistic interaction between MoS_2 and H_2O_2. The stability of OH$^\bullet$ on the 1T' phase *and* not on the 2H phase can be traced back to the metallic and semiconducting character, respectively, apparent in the density of states (DOS) projected into the MoS_2 and OH$^\bullet$ states in Figure 8c,d. The metallic character of the 1T' phase contributes to the partial quenching and delocalization of unpaired electrons, whereas they remain as well-localized electrons near the Fermi level on the semiconducting substrate.

The DCM activity of MoS_2 is therefore driven by the formation of OH$^\bullet$, which is evident in the electron transfer and structural changes in MoS_2 in the presence of H_2O_2. This could indicate that the reaction over MoS_2 is selective to a Fenton-type activation pathway, where OH$^\bullet$ formation governs interaction with CH_4, possibly both on the surface of MoS_2 or released into the surrounding liquid phase [48]. Aqueous radicals, such as $(H_2O)_2^+$, have a strong propensity to activate methane in the liquid phase even without the presence of a catalyst, able to do so in solution alone [49]. However, there is also a direct interaction between CH_4 and the MoS_2 electronic structure, as evidenced by the reduction and hybridization present in the Mo (Figure 6b) and S (Figure 7b) K-edges, when CH_4 is introduced.

3 | Conclusion

We have demonstrated the synergistic relationship between MoS_2 and H_2O_2 in directly converting CH_4 to liquid oxygenates under mild conditions, and the critical role of OH$^\bullet$ produced from H_2O_2. We report unitary selective oxygenate production that is significantly enhanced over MoS_2 by the inclusion of H_2O_2, which simultaneously activates the MoS_2 catalyst and oxidizes methane groups to form methanol and methylperoxide. MoS_2 readily decomposes H_2O_2 into OH$^\bullet$, and MoS_2 treated in similarly diluted H_2O_2 has previously been reported to greatly improve conductivity, which is consistent with the preceding [25, 26].

We suggest that this occurs due to a partial transformation to the more conductive 1T' phase of MoS_2, which experiences significantly improved electron transfer and a lower activation barrier to methane compared with the bulk, semiconducting 2H phase, allowing it to outperform nanoscale MoS_2 under similar conditions. The product (CH_3OH, CH_3OOH) is dependent upon the concentration of $OH^{\bullet}$, with higher radical concentrations favoring the peroxide form. This yields a conversion activity that is an order of magnitude greater than precious metal-based catalysts tested under similar conditions [5]. In situ activation of bulk MoS_2 material circumvents a number of processing steps, offering a more robust and cost-effective route toward direct CH_4 conversion and a significant step toward commercial CH_4 utilization.

Author Contributions

Conceptualization: SLF, ES, SDS. chemistry experiments: SLF, JDJ, AXC. beamline experiments: SLF, JDJ, DW, AT, JM, AMA. DFT calculations: ET, AB. raman experiments: SMM, MKK. in situ NMR, EPR: JZ, YL, LQ, UK. XPS: AI. microscopy and imaging: JL. writing – original draft: SLF. writing – review and editing: SLF, JDJ, DW, ES, SDS.

Acknowledgements

Work carried out at Brookhaven National Laboratory (BNL) was supported by the U.S. Department of Energy (DOE), Office of Science, Office of Basic Energy Sciences, Chemical Sciences, Geosciences, and Biosciences (CSGB) Division, Catalysis Science Program under contract no. DE-SC0012704. SLF and JDJ acknowledge support from the BNL Goldhaber Distinguished Fellowship. This research used resources of the 8-ID (ISS), 8-BM (TES), and 28-ID-1 (PDF) beamlines of the National Synchrotron Light Source II, a DOE Office of Science User Facility operated by BNL under Contract No. DE-SC0012704. AXC acknowledges support from the Office of Workforce Development for Teachers and Scientists (WDTS) under the U.S. DOE Science Undergraduate Laboratory Internships (SULI) program. A portion of this work was supported by the donors of ACS Petroleum Research Fund under Grant 66593-ND5. AS served as Principal Investigator on ACS PRF 66593-ND5. JL is a Serra Húnter Fellow and gratefully acknowledges support from the Academia Excellence Award (Generalitat de Catalunya), project MICIN/FEDER PID2024-156765OB-C21, and the Maria de Maeztu Units of Excellence Programme CEX2023-001300-M, funded by MCIN/AEI 10.13039/501100011033. The authors acknowledge the use of instrumentation provided by the Joint Electron Microscopy Center at ALBA (JEMCA). LQ, YL, and JZ were supported by the DOE, Office of Science, Office of Basic Energy Sciences, CSGB Division, Catalysis Science program. Ames National Laboratory is operated for the DOE by Iowa State University under Contract No. DEAC02-07CH11358. LQ, YL, JZ, and UK thank the support from Iowa State University. AB and ET acknowledge support from the MCIN/AEI (PID2022-140120OA-I00, CEX2021-001202-M and RYC2021-032281-I). This study was also supported by the COST Action CA21101. Computational time was kindly provided by the *Red Española de Supercomputación*.

Funding

Work carried out at Brookhaven National Laboratory (BNL) was supported by the U.S. Department of Energy (DOE), Office of Science, Office of Basic Energy Sciences, Chemical Sciences, Geosciences, and Biosciences (CSGB) Division, Catalysis Science Program under contract no. DE-SC0012704. SLF and JDJ acknowledge support from the BNL Goldhaber Distinguished Fellowship. This research used resources of the 8-ID (ISS), 8-BM (TES), and 28-ID-1 (PDF) beamlines of the National Synchrotron Light Source II, a DOE Office of Science User Facility operated by BNL under Contract No. DE-SC0012704. AXC acknowledges support from the Office of Workforce Development for Teachers and Scientists (WDTS) under the U.S. DOE Science Undergraduate Laboratory Internships (SULI) program. A portion of this work was supported by the donors of ACS Petroleum Research Fund under Grant 66593-ND5. AS served as Principal Investigator on ACS PRF 66593-ND5. JL is a Serra Húnter Fellow and gratefully acknowledges support from the Academia Excellence Award (Generalitat de Catalunya), project MICIN/FEDER PID2024-156765OB-C21, and the Maria de Maeztu Units of Excellence Programme CEX2023-001300-M, funded by MCIN/AEI 10.13039/501100011033. The authors acknowledge the use of instrumentation provided by the Joint Electron Microscopy Center at ALBA (JEMCA). LQ, YL, and JZ were supported by the DOE, Office of Science, Office of Basic Energy Sciences, CSGB Division, Catalysis Science program. Ames National Laboratory is operated for the DOE by Iowa State University under Contract No. DEAC02-07CH11358. LQ, YL, JZ, and UK thank the support from Iowa State University. AB and ET acknowledge support from the MCIN/AEI (PID2022-140120OA-I00, CEX2021-001202-M and RYC2021-032281-I). This study was also supported by the COST Action CA21101. Computational time was kindly provided by the *Red Española de Supercomputación*.

Conflicts of Interest

The authors declare no conflicts of interest.

Data Availability Statement

The data that support the findings of this study are available from the corresponding author upon reasonable request.

References

1. P. Tomkins, M. Ranocchiari, and J. A. van Bokhoven, "Direct Conversion of Methane to Methanol under Mild Conditions over Cu-Zeolites and beyond," *Accounts of Chemical Research* 50, no. 2 (2017): 418–425, https://doi.org/10.1021/acs.accounts.6b00534.

2. N. R. Foster, "Direct Catalytic Oxidation of Methane to Methanol A Review," *Applied Catalysis* 19, no. 1 (1985): 1–11, https://doi.org/10.1016/S0166-9834(00)82665-2.

3. C. D. Elvidge, M. Zhizhin, K. Baugh, F.-C. Hsu, and T. Ghosh, "Methods for Global Survey of Natural Gas Flaring from Visible Infrared Imaging Radiometer Suite Data," *Energies* 9, no. 1 (2016): 14, https://doi.org/10.3390/en9010014.

4. Z. Liu, E. Huang, I. Orozco, et al., "Water-promoted Interfacial Pathways in Methane Oxidation to Methanol on a CeO_2-Cu_2O Catalyst," *Science* 368, no. 6490 (2020): 513–517, https://doi.org/10.1126/science.aba5005.

5. J. D. Jiménez, P. G. Lustemberg, M. Danielis, et al., "From Methane to Methanol: Pd-iC-CeO_2 Catalysts Engineered for High Selectivity via Mechanochemical Synthesis," *Journal of the American Chemical Society* 146, no. 38 (2024): 25986–25999, https://doi.org/10.1021/jacs.4c04815.

6. K. Zhu, S. Liang, X. Cui, et al., "Highly Efficient Conversion of Methane to Formic Acid under Mild Conditions at ZSM-5-confined Fe-sites," *Nano Energy* 82 (2021): 105718, https://doi.org/10.1016/j.nanoen.2020.105718.

7. F. Ni, T. Richards, L. R. Smith, et al., "Selective Oxidation of Methane to Methanol via in Situ H_2O_2 Synthesis," *ACS Organic & Inorganic Au* 3, no. 4 (2023): 177–183, https://doi.org/10.1021/acsorginorgau.3c00001.

8. J. Zhu, V. L. Sushkevich, A. J. Knorpp, et al., "Cu-Erionite Zeolite Achieves High Yield in Direct Oxidation of Methane to Methanol by Isothermal Chemical Looping," *Chemistry of Materials* 32, no. 4 (2020): 1448–1453, https://doi.org/10.1021/acs.chemmater.9b04223.

9. R. Horn and R. Schlögl, "Methane Activation by Heterogeneous Catalysis," *Catalysis Letters* 145 (2015): 23–39, https://doi.org/10.1007/s10562-014-1417-z.

10. K. T. Dinh, M. M. Sullivan, P. Serna, R. J. Meyer, M. Dincă, and Y. Román-Leshkov, "Viewpoint on the Partial Oxidation of Methane to Methanol Using Cu- and Fe-Exchanged Zeolites," *ACS Catalysis* 8, no. 9 (2018): 8306–8313, https://doi.org/10.1021/acscatal.8b01180.

11. S. Faramawy, T. Zaki, and A. A.-E. Sakr, "Natural Gas Origin, Composition, and Processing: a Review," *Journal of Natural Gas Science and Engineering* 34 (2016): 34–54, https://doi.org/10.1016/j.jngse.2016.06.030.

12. A. Shamsi, "Partial Oxidation of Methane and the Effect of Sulfur on Catalytic Activity and Selectivity," *Catalysis Today* 139, no. 4 (2009): 268–273, https://doi.org/10.1016/j.cattod.2008.03.033.

13. S. Mokhatab, W. A. Poe, and J. G. Speight, "Chapter 7: Acid Gas Treating," *Handbook of Natural Gas Transmission and Processing* (Elsevier, 2006), 261–294.

14. W. Arabczyk, D. Moszyński, U. Narkiewicz, P. Pelka, and M. Podsiadły, "Poisoning of Iron Catalyst by Sulfur," *Catalysis Today* 124, no. 1-2 (2007): 43–48, https://doi.org/10.1016/j.cattod.2007.02.003.

15. B. H. Danziger, "Catalysts," *Industrial & Engineering Chemistry* 47, no. 8 (1955): 1495–1500, https://doi.org/10.1021/ie50548a019.

16. V. P. Pham and G. Y. Yeom, "Recent Advances in Doping of Molybdenum Disulfide: Industrial Applications and Future Prospects," *Advanced Materials* 28, no. 41 (2016): 9024–9059, https://doi.org/10.1002/adma.201506402.

17. S. L. Farrell, M. Khwaja, I. J. Paredes, et al., "Elucidating Local Structure and Positional Effect of Dopants in Colloidal Transition Metal Dichalcogenide Nanosheets for Catalytic Hydrogenolysis," *The Journal of Physical Chemistry C* 128, no. 11 (2024): 4470–4482, https://doi.org/10.1021/acs.jpcc.3c07408.

18. B. Seo, G. Y. Jung, Y. J. Sa, et al., "Monolayer-Precision Synthesis of Molybdenum Sulfide Nanoparticles and Their Nanoscale Size Effects in the Hydrogen Evolution Reaction," *ACS Nano* 9, no. 4 (2015): 3728–3739, https://doi.org/10.1021/acsnano.5b00786.

19. X. Diao and N. Ji, "Rational Design of MoS_2-based Catalysts toward Lignin Hydrodeoxygenation: Interplay of Structure, Catalysis, and Stability," *Journal of Energy Chemistry* 77 (2023): 601–631, https://doi.org/10.1016/j.jechem.2022.11.056.

20. J. Gao, Y. Zheng, J.-M. Jehng, Y. Tang, I. E. Wachs, and S. G. Podkolzin, "Identification of Molybdenum Oxide Nanostructures on Zeolites for Natural Gas Conversion," *Science* 348, no. 6235 (2015): 686–690, https://doi.org/10.1126/science.aaa7048.

21. J. Mao, H. Liu, X. Cui, et al., "Direct Conversion of Methane with O_2 at Room Temperature over Edge-rich MoS_2," *Nature Catalysis* 6 (2023): 1052–1061, https://doi.org/10.1038/s41929-023-01030-2.

22. Z. Wang, Q. Li, H. Xu, et al., "Controllable Etching of MoS_2 Basal Planes for Enhanced Hydrogen Evolution through the Formation of Active Edge Sites," *Nano Energy* 49 (2018): 634–643, https://doi.org/10.1016/j.nanoen.2018.04.067.

23. J. Kibsgaard, Z. Chen, B. N. Reinecke, and T. F. Jaramillo, "Engineering the Surface Structure of MoS_2 to Preferentially Expose Active Edge Sites for Electrocatalysis," *Nature Materials* 11 (2012): 963–969, https://doi.org/10.1038/nmat3439.

24. Y. Yu, L. Lu, Q. Yang, A. Zupanic, Q. Xu, and L. Jiang, "Using MoS_2 Nanomaterials to Generate or Remove Reactive Oxygen Species: a Review," *ACS Appl Nano Mater* 4, no. 8 (2021): 7523–7537, https://doi.org/10.1021/acsanm.1c00751.

25. Q. Li, B. Hu, Q. Yang, et al., "Interaction Mechanism between Multi-layered MoS_2 and H_2O_2 for Self-generation of Reactive Oxygen Species," *Environmental Research* 191 (2020): 110227, https://doi.org/10.1016/j.envres.2020.110227.

26. D. Saha, P. R. Selvanganapathy, and P. Kruse, "Peroxide-Induced Tuning of the Conductivity of Nanometer-Thick MoS_2 Films for Solid-State Sensors," *ACS Applied Nano Materials* 3, no. 11 (2020): 10864–10877, https://doi.org/10.1021/acsanm.0c02135.

27. P. Chowdhury, A. Roy, and S. Ghosh, "Molybdenum Disulfide Nanomaterials for Generating or Depleting Reactive Oxygen Species: Recent Development and Prospects in Biomedical Applications," *Small* 21, no. 38 (2025): 06450, https://doi.org/10.1002/smll.20250450.

28. S. L. Farrell, N. Osinski, I. J. Paredes, et al., "Basal Plane Doping to Activate Colloidal MoS_2 Nanosheets for Catalytic Hydrodeoxygenation of *Para*-Cresol," *ACS Applied Materials & Interfaces* 18, no. 14 (2026): 20838–20847, https://doi.org/10.1021/acsami.5c24853.

29. J. Kiepe, S. Horstmann, K. Fischer, and J. Gmehling, "Experimental Determination and Prediction of Gas Solubility Data for Methane + Water Solutions Containing Different Monovalent Electrolytes," *Industrial & Engineering Chemistry Research* 42 (2003): 5392–5398, https://doi.org/10.1021/ie030386x.

30. S. Al-Shihri, C. J. Richard, and D. Chadwick, "Selective Oxidation of Methane to Methanol over ZSM-5 Catalysts in Aqueous Hydrogen Peroxide: Role of Formaldehyde," *Chemcatchem* 9, no. 7 (2017): 1276–1283, https://doi.org/10.1002/cctc.201601563.

31. R. McVicker, N. Agarwhal, S. J. Freakley, et al., "Low Temperature Selective Oxidation of Methane Using Gold-palladium Colloids," *Catalysis Today* 342 (2020): 32–38, https://doi.org/10.1016/j.cattod.2018.12.017.

32. M. H. Ab Rahim, M. M. Forde, R. L. Jenkins, et al., "Oxidation of Methane to Methanol with Hydrogen Peroxide Using Supported Gold-Palladium Alloy Nanoparticles," *Angewandte Chemie International Edition* 52, no. 4 (2012): 1280–1284, https://doi.org/10.1002/anie.201207717.

33. K. Makino, A. Hagi, H. Ide, A. Murakami, and M. Nishi, "Mechanistic Studies on the Formation of Aminoxyl Radicals from 5,5-dimethyl-1-pyrroline-*N*-oxide in Fenton Systems. Characterization of Key Precursors Giving Rise to Background ESR Signals," *Canadian Journal of Chemistry* 70 (1992): 2818–2827, https://doi.org/10.1139/v92-358.

34. J. M. Fontmorin, R. C. Burgos Castillo, W. Z. Tang, and M. Sillanpää, "Stability of 5,5-dimethyl-1-pyrroline-*N*-oxide as a Spin-trap for Quantification of Hydroxyl Radicals in Processes Based on Fenton Reaction," *Water Research* 99 (2016): 24–32, https://doi.org/10.1016/j.watres.2016.04.053.

35. L. Li, Q. Wu, S.-K. Xiang, et al., "Electron Paramagnetic Resonance Tracks Condition-Sensitive Water Radical Cation," *The Journal of Physical Chemistry Letters* 14, no. 41 (2023): 9183–9191, https://doi.org/10.1021/acs.jpclett.3c02268.

36. M. Li, J. Shan, G. Giannakakis, et al., "Single-step Selective Oxidation of Methane to Methanol in the Aqueous Phase on Iridium-based Catalysts," *Applied Catalysis B: Environmental* 292 (2021): 120124, https://doi.org/10.1016/j.apcatb.2021.120124.

37. Y. Kwon, T. Y. Kim, G. Kwon, J. Yi, and H. Lee, "Selective Activation of Methane on Single-Atom Catalyst of Rhodium Dispersed on Zirconia for Direct Conversion," *Journal of the American Chemical Society* 139, no. 48 (2017): 17694–17699, https://doi.org/10.1021/jacs.7b11010.

38. L. Dong, S. Lin, L. Yang, et al., "Spontaneous Exfoliation and Tailoring of MoS_2 in Mixed Solvents," *Chemical Communications* 50, no. 100 (2014): 15936–15939, https://doi.org/10.1039/C4CC07238C.

39. X. Tian, J. Wu, Q. Li, et al., "Scalable Production of Few-layer Molybdenum Disulfide Nanosheets by Supercritical Carbon Dioxide," *Journal of Materials Science* 53 (2018): 7258–7265, https://doi.org/10.1007/s10853-018-2053-6.

40. Z. J. Yang, Z. Li, L. Loh, et al., "Scalable Manufacture of Nearly Pure-phase Metallic MoS_2 Nanosheets," *Nature Materials*, ahead of print, January 29, 2026, https://doi.org/10.1038/s41563-026-02480-2.

41. Z. Li, Q. He, T. H. Tran, et al., "Metastable 1T′-phase Group VIB Transition Metal Dichalcogenide Crystals," *Nature Materials* 20 (2021): 1113–1120, https://doi.org/10.1038/s41563-021-00971-y.

42. Y. Yao, H. Cumberbatch, D. D. Robertson, M. A. Chin, R. Lamkin, and S. H. Tolbert, "On the Interplay between Size and Disorder in Suppressing Intercalation-Induced Phase Transitions in Pseudocapacitive

Nanostructured MoS_2," *Advanced Functional Materials* 34, no. 50 (2023): 2304896, https://doi.org/10.1002/adfm.202304896.

43. B. Schönfeld, J. J. Huang, and S. C. Moss, "Anisotropic mean-square displacements (MSD) in single-crystals of 2H-and 3R-MoS_2," *Structural Science* 39 (1983): 404–407, https://doi.org/10.1107/S0108768183002645.

44. C. D. Quilty, L. M. Housel, D. C. Bock, et al., "Ex Situ and Operando XRD and XAS Analysis of MoS_2: A Lithiation Study of Bulk and Nanosheet Materials," *ACS Applied Energy Materials* 2, no. 10 (2019): 7635–7646, https://doi.org/10.1021/acsaem.9b01538.

45. L. Cai, W. Cheng, T. Yao, et al., "High-Content Metallic 1T Phase in MoS_2-Based Electrocatalyst for Efficient Hydrogen Evolution," *The Journal of Physical Chemistry C* 121, no. 28 (2017): 15071–15077, https://doi.org/10.1021/acs.jpcc.7b03103.

46. Q. Liu, X. Li, Q. He, et al., "Gram-Scale Aqueous Synthesis of Stable Few-Layered 1T-MoS_2: Applications for Visible-Light-Driven Photocatalytic Hydrogen Evolution," *Small* 11, no. 41 (2015): 5556–5564, https://doi.org/10.1002/smll.201501822.

47. A. T. Garcia-Esparza, S. Park, H. Abroshan, et al., "Local Structure of Sulfur Vacancies on the Basal Plane of Monolayer MoS_2," *ACS Nano* 16 (2022): 6725–6733, https://doi.org/10.1021/acsnano.2c01388.

48. A. Szécsényi, G. Li, J. Gascon, and E. A. Pidko, "Mechanistic Complexity of Methane Oxidation with H_2O_2 by Single-Site Fe/ZSM-5 Catalyst," *ACS Catalysis* 8 (2018): 7961–7972, https://doi.org/10.1021/acscatal.8b01672.

49. X. Zhang, R. Su, M. Duan, et al., "Ambient Catalyst-free Conversion of Methane to Methanol by Water Radical Cations," *Science Advances* 11, no. 31 (2025): adw0584, https://doi.org/10.1126/sciadv.adw0584.

Supporting Information

Additional supporting information can be found online in the Supporting Information section.

Supporting File: adfm76526-sup-0001-SuppMat.docx.